

# {110} planar faults in strained bcc metals: Origins and implications of a commonly observed artifact of classical potentials

Johannes J. Möller,<sup>1,2,\*</sup> Matous Mrovec,<sup>3</sup> Ivan Bleskov,<sup>4</sup> Jörg Neugebauer,<sup>4</sup> Thomas Hammerschmidt,<sup>3</sup> Ralf Drautz,<sup>3</sup> Christian Elsässer,<sup>2,5</sup> Tilmann Hickel,<sup>4</sup> and Erik Bitzek<sup>1</sup>

<sup>1</sup>Friedrich-Alexander-Universität Erlangen-Nürnberg, Department of Materials Science and Engineering, Institute I, Martensstr. 5, D-91058 Erlangen, Germany

<sup>2</sup>Fraunhofer Institute for Mechanics of Materials IWM, Wöhlerstr. 11, D-79108 Freiburg, Germany

<sup>3</sup>Interdisciplinary Centre for Advanced Materials Simulation,

Ruhr-University Bochum, Universitätsstr. 150, D-44780 Bochum, Germany

<sup>4</sup>Computational Materials Design, Max-Planck-Institut für Eisenforschung GmbH, Max-Planck-Str. 1, D-40237 Düsseldorf, Germany

<sup>5</sup>University of Freiburg, Freiburg Materials Research Center, Stefan-Meier-Str. 21, D-79104 Freiburg, Germany

Large-scale atomistic simulations with classical potentials can provide valuable insights into microscopic deformation mechanisms and defect-defect interactions in materials. Unfortunately, these assets often come with the uncertainty of whether the observed mechanisms are based on realistic physical phenomena or whether they are artifacts of the employed material models. One such example is the often reported occurrence of stable planar faults (PFs) in body-centered cubic (bcc) metals subjected to high strains, e.g., at crack tips or in strained nano-objects. In this paper, we study the strain dependence of the generalized stacking fault energy (GSFE) of {110} planes in various bcc metals with material models of increasing sophistication, i.e., (modified) embedded atom method, angular-dependent, Tersoff, and bond-order potentials as well as density functional theory. We show that under applied tensile strains the GSFE curves of many classical potentials exhibit a local minimum which gives rise to the formation of stable PFs. These PFs do not appear when more sophisticated material models are used and have thus to be regarded as artifacts of the potentials. We demonstrate that the local GSFE minimum is not formed for reasons of symmetry and we recommend including the determination of the strain-dependent (110) GSFE as a benchmark for newly developed potentials.

## I. INTRODUCTION

Atomic-scale modeling of materials can provide fundamental information about microscopic deformation mechanisms and defect-defect interactions [1], which can ultimately stimulate the development of higher-scale models with input parameters from atomistic simulations [2, 3]. At the same time, results of atomic-level simulations are often subject to some uncertainty, particularly in case of classical molecular dynamics (MD) simulations. This uncertainty mainly arises from the question whether the interatomic potential employed in the simulations correctly reflects the material's response to the applied loads. However, studies of plastic deformation and fracture necessitate the simulation of many millions of atoms [4–7], where classical interatomic models are without alternatives. To check if the performed simulations are independent of the used material model is therefore of prior importance for the transferability and acceptance of the obtained results. It is important to note that the common approach to only compare different potentials of the same type is generally not sufficient as all potentials of the same type might suffer from the same problems.

In this paper, we use various well-established material models to determine the strain-dependent generalized stacking fault energy (GSFE) curves for body-centered cubic (bcc) transition metals. The GSFE (also known as "γ surface") [8] is determined by rigidly shifting two half crystals with respect to each other, typically under stress-free boundary conditions.

Local GSFE minima and maxima indicate stable (and unstable) stacking faults (SSFs), respectively. Whether a material has a local GSFE minimum can be theoretically inferred from its crystal symmetry. This principle, which was originally established by Neumann [9], states that GSFE minima are only possible where two non-parallel symmetry planes intersect the crystal's glide plane. Unlike bcc materials, face-centered cubic (fcc) crystals contain such crossings of symmetry planes in their slip planes and therefore exhibit SSFs. Despite the idealized nature of the GSFE, the presence of SSFs, their energies, and relation to the unstable stacking fault energy turned out to be a good indicator for the nature of the material's slip behavior [10–12]. This is especially evident for materials with local GSFE minima, such as the fcc metals Al, Cu, and Ni, for which Brandl *et al.* [13] have already determined the strain-dependent GSFEs for isotropic and simple shear strains. The strain dependence of the GSFE in bcc crystals, however, is still unknown.

For unstrained bcc crystals, it has been known for a long time that the formation of SSFs by dislocation dissociation is not possible [8]. However, for situations where the elastic stress state deviates strongly from stress-free conditions this common conception needs not to be valid. In such extreme scenarios, e.g., at crack tips or in nanostructures, the following dislocation dissociation might therefore be possible [14]:

$$\frac{a_0}{2}[1\bar{1}1] \rightarrow \frac{a_0}{8}[1\bar{1}0] + \frac{a_0}{4}[1\bar{1}2] + \frac{a_0}{8}[1\bar{1}0] \quad (1)$$

This possibility has been theoretically proposed and discussed by a number of research groups in the early 1960s [14–19] based on hard-sphere models. Additionally, some experimental studies indeed gave an indication for the existence of dissociated dislocations on {110} planes in Fe [20] and Nb [21].

\* Corresponding author: johannes.moeller@iwm.fraunhofer.de

More than two decades after these experimental works, the formation of PFs has now been observed in atomistic simulations of highly strained systems, e.g., at straight crack tips [22–27], highly curved, penny-shaped crack fronts [28, 29], and nanobeams subjected to bending [30] and tension [31] as well as containing notches [32]. The formation of PFs at straight crack tips is exemplified in Figs. 1(a) and 1(b) for two different embedded atom method (EAM) potentials for Fe. Whereas for the Chamati potential [33], Fig. 1(a), no extended planar defects appear on  $\{110\}$  planes (inclined by  $\pm 45^\circ$ ), these defects are clearly visible (green colored atoms) for the Mendeleev-II potential [34]; Fig. 1(b). Upon further loading, the cracks modeled with the Chamati potential propagate on the original (100) crack plane whereas with the Mendeleev-II potential the crack kinks onto one of the inclined  $\{110\}$  planes [26]. Examples for the formation of PFs at curved crack fronts and in bent nanowires are provided in the [Supplemental Material]. An earlier work of some of the authors [26] has shown that for many semi-empirical interatomic potentials of the EAM type [35, 36], the formation of these unexpected PFs can be traced back to the strain-induced formation of a local GSF E minimum at relative displacements of approximately  $a_0/6[1\bar{1}0]$ , which is in the range of the proposed displacement vector in Eq. (1).

The atomistic configurations in Figs. 1(a) and 1(b) are analyzed using the bcc defect analysis (BDA) [37] that was specifically developed to distinguish common defects in bcc structures. In contrast, the well-known common neighbor analysis (CNA) [39], which was used in many of the references above [22–32], identifies the defective regions as belonging to the fcc crystal structure, cf. Figs. 1(c) and 1(d). A detailed analysis of the defect structures, however, reveals that the  $\{110\}$  habit plane of the defects is still closer to  $\{110\}_{\text{bcc}}$  planes than to  $\{111\}_{\text{fcc}}$  planes. This can clearly be seen by directly comparing the defective regions for the two potentials in Figs. 1(e)–1(h). The misclassification as fcc explains why PFs were often not labeled as such and instead discussed in the context of  $\text{bcc} \rightarrow \text{fcc}$  transformations [22–24, 27], such as the inverse Bain path [40]. We will therefore refer to this defect type only as “planar faults” (PF) in the following. The reader should, however, keep in mind that the same type of planar defects might be labeled as “fcc formation elsewhere.

The objective of this paper is to clarify if there is a physical reason for the strain-dependent formation of PFs in bcc metals. For this purpose, we determine the  $(110)$  GSF E in the  $[1\bar{1}0]$  and  $[1\bar{1}1]$  directions (so-called “ $\gamma$  lines” or “1D GSF E profiles”) for systematically varied strain states using different EAM-type potentials as well as several atomistic material models with increasingly sophisticated descriptions of the bonding situations: Modified EAM (MEAM) potentials, angular-dependent potentials (ADPs), Tersoff potentials, bond-order potentials (BOPs), and density functional theory (DFT). Table I summarizes the contributions for modeling atomic interactions that are explicitly included or not taken into account in the different material models. Knowledge about the underlying physical reason for the formation of bcc PFs is of fundamental importance for the reliability of the results and conclusions in Refs. [22–26, 28–32], their transfer-

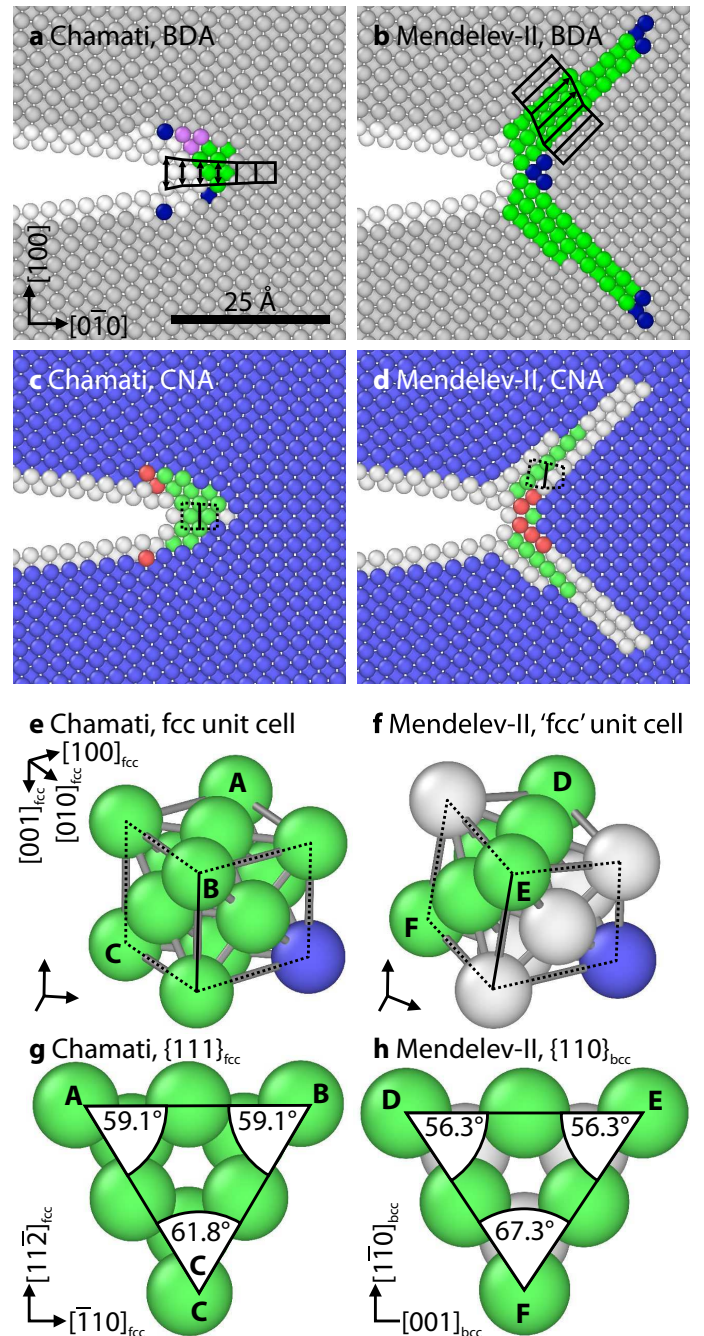


FIG. 1. Comparison of atomistic configurations in Fe modeled with the Chamati (left, no PF formation) and Mendeleev-II potentials (right, PF formation), see Ref. [26] for details. (a) and (b),  $(100)[001]$  crack system directly before brittle fracture, in BDA [37, 38] coloring (grey: bulk; white: surface; green:  $\{110\}$  PFs; blue: non-screw dislocation), the main deformation paths are marked with black lines; (c) and (d), same configurations in CNA [39] coloring (blue: bcc; green: fcc; red: hcp; white: other); (e) and (f), possible fcc unit cells extracted from the marked regions in (c) and (d); (g) and (h), top views on possible  $\{111\}_{\text{fcc}}$  planes extracted from the unit cells in (e) and (f); the characteristic angles between possible  $\langle 110 \rangle_{\text{fcc}}$  bonds deviate less than  $2^\circ$  from the ideal fcc angles for the Chamati potential ( $\angle ABC = \angle BCA = \angle CAB = 60^\circ$ ); for the Mendeleev-II potential, the characteristic angles are still closer to the ideal bcc values ( $\angle DEF = \angle FDE \approx 54.7^\circ$ ,  $\angle EFD \approx 70.5^\circ$ ), where the maximum deviation is less than  $4^\circ$  (maximum deviation from the characteristic fcc angles  $> 7^\circ$ ).

TABLE I. Summary of contributions for modeling atomic interactions explicitly included (●) or not taken into account (○) in the different material models.

Model	Radial distance	Directional bonding	Bond order	Magnetism	Electronic structure
EAM/FS	●	○	○	○	○
MEAM	●	●	○	○	○
ADP	●	●	○	○	○
Tersoff	●	●	●	○	○
BOP	●	●	●	●	○ <sup>a</sup>
DFT	●	●	●	●	●

<sup>a</sup> Basic electronic structure captured

ability to higher scales [41–43], and the development of new interatomic potentials for bcc metals [44].

The paper is organized as follows: in Sec. II, we introduce the various computational methods for determining  $\gamma$  surfaces and  $\gamma$  lines. The simulation results are presented in Sec. III. The discussion in Sec. IV focuses on possible explanations for the strain-dependent formation of a local GSFE minimum for EAM-type potentials and how this might be prevented during potential fitting. Finally, a brief summary of the paper is given in Sec. V.

## II. METHODS

The 1D  $\{110\}$  GSFE profiles ( $\gamma$  lines) along  $[1\bar{1}0]$  and  $[1\bar{1}1]$  directions were determined as functions of different uniaxial and equi-biaxial strains in various bcc metals. The setup geometries are described in Sec. II A. For Fe, different material models with increasing complexity were used: EAM, MEAM, ADP, Tersoff, BOP, and DFT. For the other bcc metals, EAM potentials were compared to DFT. The main concepts of the different models are described in Secs. II B–II G. Table I provides a comprehensive summary of the different contributions for modeling atomic interactions that are explicitly included in the models.

### A. Setup geometries

Uniaxial strains (US) are applied normal to the PF plane in the range  $\varepsilon_{[110]} = 0.0\text{--}10.0\%$  (tension) with strain increments of  $\Delta\varepsilon = 1.0\%$ . Equi-biaxial strains (EBS) contain an equally high additional strain component in  $[1\bar{1}0]$  direction, i.e.,  $\varepsilon_{[1\bar{1}0]} = \varepsilon_{[110]}$ . Both strain ranges and directions are chosen to model the high strains that are present at a crack tip; see e.g., Fig. 1.

Figure 2 displays two different setup geometries for determining the  $\gamma$  surfaces and the  $\gamma$  lines. The “large” setup in Fig. 2(a) is primarily suited for simulations using classical potentials (Secs. II B–II E). It contains hundreds to thousands of atoms and fulfills the minimum image convention, namely that the box sizes within the PF plane are larger than  $2r_{\text{cut}}$ .

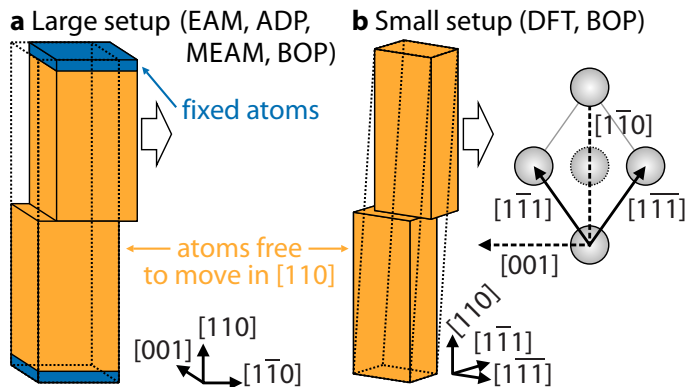


FIG. 2. Simulation setups for determining  $\gamma$  surfaces and  $\gamma$  lines. The large setup (a) is periodic in  $[1\bar{1}0]$  and  $[001]$  directions with fixed regions at the top and bottom in the  $[110]$  direction; the box size is larger than  $2r_{\text{cut}}$  ( $r_{\text{cut}}$ , cutoff radius of the respective potential) in periodic directions and approximately 60 unit cells along the long axis; typical simulation boxes consist of hundreds to thousands of atoms and are used in simulations with classical interatomic potentials. The small setup [45, 46] (b) is periodic in all box directions (dotted lines); the box size is each one  $\langle 111 \rangle$  periodicity distance along the two short box axes and eight periodicity distances along the long  $[110]$  direction; the box contains usually tens of atoms and is suited for DFT calculations (and simulations using BOPs for comparison); by adjusting the direction of the long box vector in each shearing step, only one stacking fault is formed in the plane where the two rigid blocks are sheared against each other. In both setups, atomic motion during the relaxation process is limited to directions perpendicular to the  $(110)$  plane.

Along these lateral box axes, periodic boundary conditions (PBC) are used. The boundary conditions in the direction perpendicular to the PF plane are non-periodic, which leads to two free surfaces at the top and bottom of the configuration. During energy minimization, the lateral box sizes are kept fixed, meaning that Poisson contraction is not allowed. Most simulation boxes are constructed such that they contain  $3 \times 60 \times 4$  unit cells in the  $[1\bar{1}0]$ ,  $[110]$ , and  $[001]$  directions, respectively.

The “small” setup in Fig. 2(b) is mainly intended for the more sophisticated descriptions of atomic bonding (Secs. II F and II G). This setup is periodic in all directions and has box vectors in the  $[1\bar{1}1]$  and  $[1\bar{1}\bar{1}]$  directions. The long box vector, which is initially normal to the SF plane, is adjusted at each displacement step in such a way that the crystal structure is coherent at both ends of the simulation box. In other words, the simulation box contains only the stacking fault in the center, but no additional surface or interface at the top or bottom. The majority of the simulation boxes constructed in this manner contains  $1 \times 8 \times 1$  unit cells in the  $[1\bar{1}1]$ ,  $[110]$ , and  $[1\bar{1}\bar{1}]$  directions, respectively. Further details on this simulation setup can be found in Refs. [45, 46].

To determine the  $\gamma$  lines, one half of the crystal is displaced in incremental steps of  $1/96$  (Secs. II B–II E) and  $1/12$  (Secs. II F and II G) of the corresponding periodicity distances, i.e.,  $a_0[1\bar{1}0]$  or  $a_0/2[1\bar{1}1]$ . After each displacement step, the energy of the corresponding configuration was min-

imized using the relaxation algorithms and convergence criteria as described in the following (Secs. II B–II G). For both setup geometries, the GSFE  $\gamma$  is calculated as the difference between the total potential energy of the shifted crystal  $E^{\text{tot}}$  and the energy  $E_0^{\text{tot}}$  of the initial, undisplaced, configuration [8]:

$$\gamma = \frac{(E^{\text{tot}} - E_0^{\text{tot}})}{A_{110}} \quad (2)$$

where  $A_{110}$  is the area of the (110) plane in the simulation box. In most cases, the  $\gamma$  lines in the  $[1\bar{1}1]$  Burgers vector direction were determined for comparison.

Atomistic configurations are always visualized using OVITO [47, 48] and analyzed using the CNA [39] and the recently developed BDA [37, 38].

## B. Embedded Atom Method Potentials

According to the EAM formalism, the total potential energy  $E_{\text{pot}}^{\text{tot}}$  of an  $N$ -atom configuration is given by [35]:

$$E_{\text{pot}}^{\text{tot}} = \sum_{i=0}^N E_{\text{pair}}^i + \sum_{i=0}^N E_{\text{embed}}^i \quad (3)$$

$$E_{\text{pair}}^i = \sum_{j=0}^N \frac{1}{2} V(r_{ij}) \text{ for } j \neq i, \quad (4)$$

$$E_{\text{embed}}^i = F(\rho^i) = F\left(\sum_{j=0}^N f(r_{ij})\right) \text{ for } j \neq i. \quad (5)$$

The radial-symmetric functions,  $V(r_{ij})$  and  $f(r_{ij})$ , depend only on  $r_{ij}$ , i.e., the distance between two atoms  $i$  and  $j$  and  $\rho^i$  is the electron density at the site of atom  $i$ . The non-pairwise embedding energy term,  $F(\rho^i)$ , describes the energy contribution arising from the electron density.

In this study, we compare a variety of EAM-type potentials for Fe spanning almost 30 years of potential development: from the historic Finnis-Sinclair (FS) potential in the modified form of Marchese *et al.* [49, 50], abbreviated as "MFS", to the most recent "Marinical 1" potential by Proville *et al.* [51]. In addition, we studied the FS potentials for V, Nb, Ta, Mo, and W in the modified version of Ackland and Thetford [52], abbreviated as "ATFS". Since such an Ackland-Thetford correction does not exist for Cr, we used the original FS potential instead. For Nb, Mo and W, the additional potential parameterizations by Fellingner *et al.* [53], Ackland *et al.* [54, 55], Smirnova *et al.* [56], and Wang *et al.* [57] were used as well. All EAM potentials used in our study are listed in Table II.

In case of EAM potentials, energy minimization is performed using the software package IMD [58, 59] with the FIRE relaxator [60] until the force-norm  $\|F\|$  is below  $10^{-8}$  eV/Å.

## C. Modified Embedded Atom Method Potentials

As EAM potentials are unable to account for directional bonds, the MEAM has been developed by Baskes *et al.* [61] to account for this effect, which is specifically important for bcc metals. As in the EAM formalism, the energy is still the sum of a distance-dependent pair-potential term and an embedding-energy term that depends on the electron density  $\rho$ . Whereas in the EAM, the assumption was made that  $\rho$  is a linear superposition of spherically averaged electron densities from all neighbor atoms, in the MEAMs  $\rho$  has a more sophisticated form that incorporates directional dependence in the electron density [62]. The MEAM was extended to include second-nearest neighbor (2nn) interactions by Lee *et al.* [63], which was shown to be an important feature to simulate the behavior of bcc metals more accurately.

We use the original 2nn-MEAM potential by Lee *et al.* [63], which is also part of the Fe-Ti-C potential of Kim *et al.* [64]. In addition, two more recent parameter sets "MEAM-p" and "MEAM-T" by Lee *et al.* [65] were used. Both parameter sets have been used in the Fe parts of MEAM potentials for Fe alloys, namely for AlSiMgCuFe by Jelinek *et al.* [66] and for Fe-C by Liyanage *et al.* [67].

In case of MEAM potentials, energy minimization is performed using the software package LAMMPS [68, 69] with the FIRE relaxator [60] until the force-norm  $\|F\|$  is below  $10^{-6}$  eV/Å.

## D. Angular-Dependent Potentials

ADPs are an alternative approach to include directional bonding in the EAM formalism as proposed by Mishin *et al.* [70]. In addition to the classical EAM functions [see Eqs. (3–5)], they contain measures for the dipole and quadrupole distortions of the local atomic environment. The main difference from the MEAM formalism introduced above is that the higher-order multipoles contribute to the electron density in MEAM potentials whereas in the ADP method they contribute directly to the total energy.

Currently, ADPs are less common than MEAM potentials and available only for a few material systems [70–72]. In this paper, we use the original ADP parameterization of Mishin *et al.* [70] for Fe. However, it should be noted here that for this parameterization the values for the elastic constants are only one half of the experimental ones [73]. It is therefore not a useful description whenever the elastic material response is of interest, as, e.g., for fracture. For the ADP used here, energy minimization is performed using the same simulation details as for the EAM potentials described in Sec. II B.

## E. Tersoff Potentials

An empirical approach based on the chemical concept of bond order was developed by Tersoff [74]. Tersoff potentials are based on Morse-type pair interactions [75] whose at-

tractive parts include a function that depends on the number, strength, and angles of the interatomic bonds.

For Fe, two different Tersoff potentials were proposed, one by Müller *et al.* [76] and another by Björkas *et al.* [77]. Note that the latter potential contains a slight modification of the repulsive part of the former to yield a more realistic description of the short-range behavior between atomic nuclei. This modification by Björkas *et al.* was also used to describe the Fe-Fe bonding in the Fe-Cr-C potential by Henriksson *et al.* [78]. For both Tersoff potentials employed here, energy minimization is performed with the same simulation details as for the MEAM potentials described in Sec. II C.

### F. Bond-order Potentials

A common characteristic of all previously mentioned classical interatomic potentials is the lack of magnetic interactions. These potentials are therefore neither able to describe the broad variety of magnetic phases of Fe nor provide any information about local magnetic phenomena in the vicinity of crystal defects [79]. One of the most successful methods to overcome this shortcoming are bond-order potentials (BOPs) [80]. This family of potentials is based on the tight-binding (TB) approximation and includes a description of both the electronic structure and magnetic interactions according to the Stoner theory of itinerant magnetism [81]. For a recent review on the derivation and parameterisation of BOPs we refer the reader to Ref. [82]

BOPs represent a bridge between the classical potentials mentioned above and the more accurate but computationally more expensive DFT calculations described in the next subsection. For this reason, both small and large setup geometries, cf. Fig. 2, are compared using the "numerical" BOP for Fe by Mrovec *et al.* [79] with the computational details (OXON code [83], relaxation with FIRE [60] until the maximum force was less than 0.01 eV/Å) as described in Ref. [79]. The procedure is repeated for the small setup geometry using an analytical BOP that Ford *et al.* [84] devised from a TB model of Madsen *et al.* [85] within the framework of analytic BOPs for d-valent systems [86]. In this case, the simulations are performed using the BOPfox code [87] with damped-Newtonian relaxation until the energy difference is below 0.001 eV/atom or the maximum force is below 0.001 eV/Å.

### G. Density-Functional Theory Calculations

Most DFT calculations [88, 89] were carried out with the plane-wave code *PWscf* of the QUANTUM ESPRESSO software package [90, 91] using the Perdew-Burke-Ernzerhof (PBE) exchange-correlation functional [92], which is based on the generalized gradient approximation (GGA), and Vanderbilt-type ultrasoft pseudopotentials (USPP) [93]. DFT calculations with USPPs are expected to yield comparable results for GSFs as compared with results for the more recent projector-augmented wave (PAW) methods; see, e.g.,

Ref. [94]. The kinetic energy cutoff of the USPPs was 30 Ry for wave functions and 120 Ry for charge densities and potentials [95]. To determine the properties of magnetic Fe, spin-polarized calculations were performed. The convergence threshold for self-consistent calculations was  $10^{-8}$  Ry (approximately  $1.36 \times 10^{-7}$  eV). Shifted  $39 \times 3 \times 39$   $k$ -point meshes for Brillouin-zone integrations were generated by the Monkhorst-Pack scheme [96] and the fractional occupations of the electronic states were realized by a Gaussian broadening [97]. Atomic positions were relaxed by minimizing the atomic forces using the Broyden-Fletcher-Goldfarb-Shanno (BFGS) relaxation scheme [98] with a convergence threshold for the largest residual force component of  $10^{-3}$  Ry/Bohr (approximately  $2.6 \times 10^{-2}$  eV/Å).

To check the independence of the DFT results from the used simulation package and realizations of the external potential, we also performed DFT calculations using the Vienna Ab initio Simulation Package (VASP) [99, 100]. The simulation details used with VASP (GGA, PBE, and PAW [101]) are reported in more detail in Ref. [102]. The determined  $\gamma$  lines were in good agreement with other calculations using the VASP code and reference data from literature [94].

## III. RESULTS

The results for the occurrence of strain-dependent local minima in the calculated  $\gamma$  lines are summarized in Table II. For reference, we always compared the unstable stacking fault energies  $\gamma_{\text{ust}}$  along the  $[1\bar{1}1]$  Burgers vector direction under unstrained conditions with other published data for the corresponding interaction models. As it is indicated in the table, some of the EAM potentials exhibit a local minimum in the middle of the  $\gamma$  line in  $[1\bar{1}1]$  direction [denoted as  $\min(\gamma_{[1\bar{1}1]})$ ]. This leads to a "double hump" shape of the GSFs where there should be only one maximum (according to the predictions of the more sophisticated methods). The Gordon potential [107], for instance, was developed exactly with the purpose to suppress this unwanted feature of many EAM potentials. The remaining three columns of Table II indicate whether there is a local minimum in the corresponding  $\gamma$  line under zero strain (ZS), 7.5% uni-axial strain (US), and/or 5% equi-biaxial strain (EBS) or not. For Fe, the size independence of the results was ensured by using simulation box sizes containing 480, 2,880, and 5,760 atoms for the Mendeleev-II EAM potential, 16 and 2,880 atoms for the Mrovec BOP, and 16 and 32 atoms in case of DFT calculations.

In Fig. 3 the  $\gamma$  surfaces of Fe are shown under unstrained (a) as well as for 7.5% uniaxial strain in  $[110]$  (b) and 5% biaxial strain in the  $[1\bar{1}0]$  and  $[110]$  directions (c). Note that all GSFs data points are plotted with respect to the energy of the crystals at zero normalized shifts irrespective of their strain state. This conceals the fact that all configurations under strained conditions are of course of higher energy than those under unstrained conditions, but it allows one to compare directly their relative evolution on the same scale as also displayed in Figs. 4 and 5. While the  $\gamma$  surfaces are only shown for the popular Mendeleev-II potential [34], the  $\gamma$  lines are also

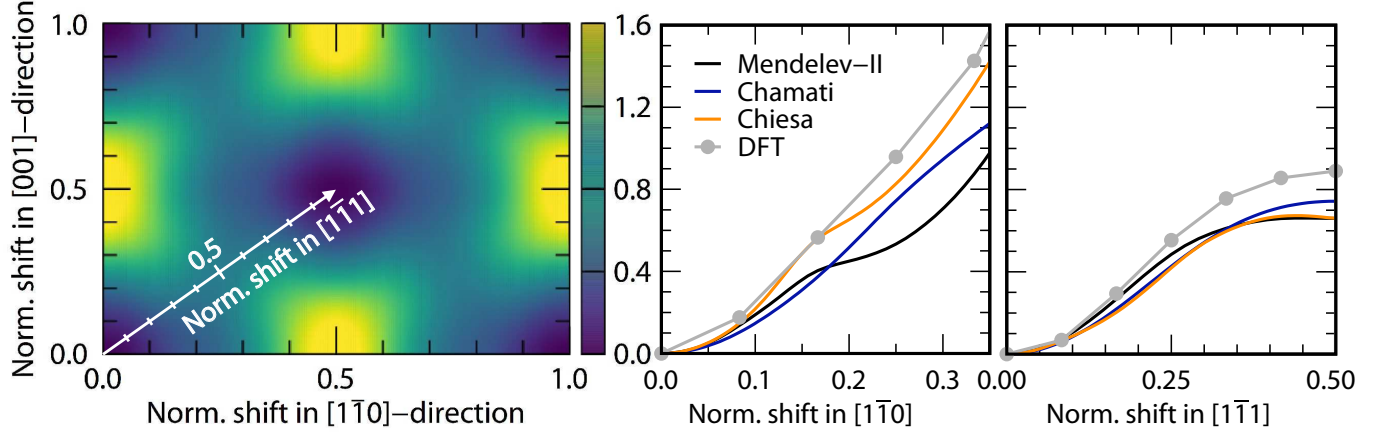
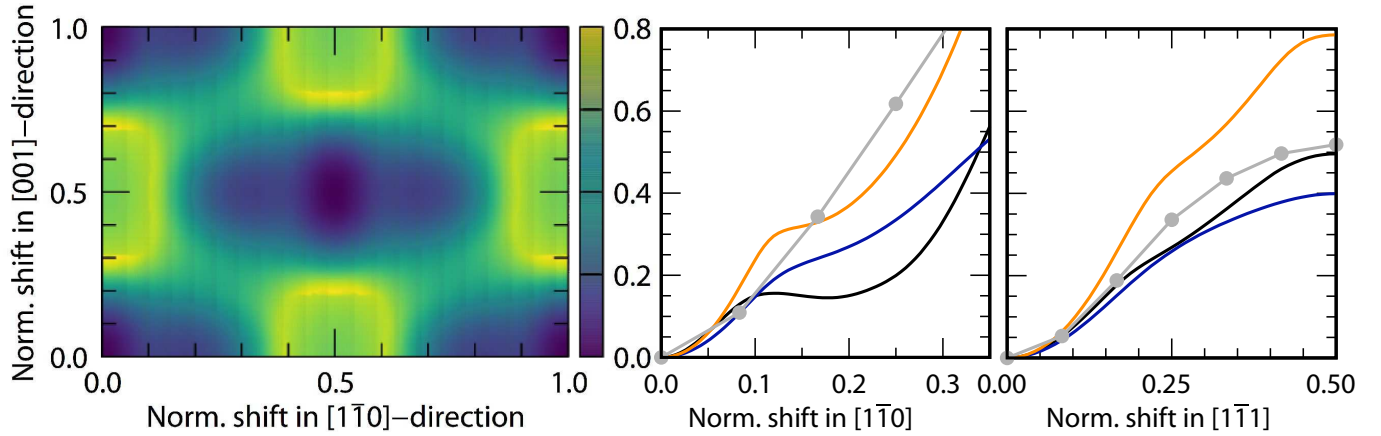
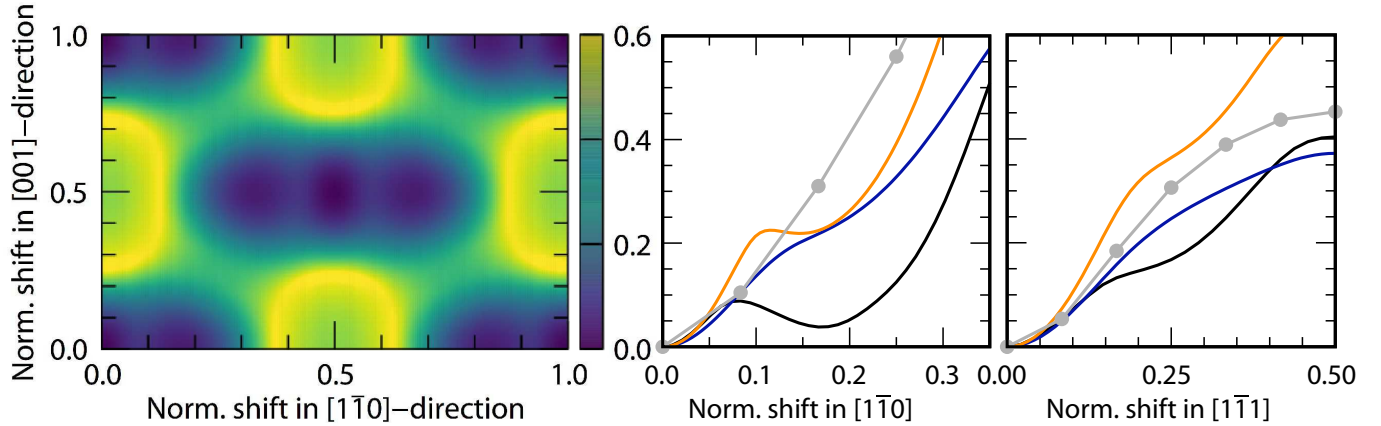
**a** Generalized stacking fault energies (GSFE) of the (110) plane ( $\text{J/m}^2$ )**b** GSFE of the (110) plane for 7.5 % uniaxial strain in [110]-direction ( $\text{J/m}^2$ )**c** GSFE of the (110) plane for 5 % equi-biaxial strain in [110]- and [1-10]-direction ( $\text{J/m}^2$ )

FIG. 3.  $\gamma$  surfaces of the (110) glide plane and corresponding 1D GSFE line profiles ( $\gamma$  lines) in  $[1\bar{1}0]$  and  $[1\bar{1}1]$  directions as function of external loads: (a) no external load; (b) 7.5 % uniaxial strain (US); (c) 5 % equi-biaxial strain (EBS). Note that the scale of the  $\gamma$  lines is the same as for the colorbars of the  $\gamma$  surfaces. The shifts in  $[001]$ ,  $[1\bar{1}0]$ , and  $[1\bar{1}1]$  directions are normalized, i.e., divided by the corresponding periodicity distances  $a_0$ ,  $\sqrt{2}a_0$ , and  $\sqrt{3}/2a_0$ . The  $\gamma$  surfaces are displayed for the Mendeleev-II potential [34]. The  $\gamma$  lines are plotted for the Mendeleev-II [34], Chamati [33], and Chiesa [104] potentials as well as for DFT calculations. All GSFE curves are plotted with respect to the energy of the crystals at zero normalized shifts irrespective of their strain state. The Mendeleev-II and Chiesa potentials tend to result in a local GSFE minimum along the  $[1\bar{1}0]$  direction under external strain [(b) and (c)]; this behavior is observed neither for the Chamati potential nor in DFT calculations.

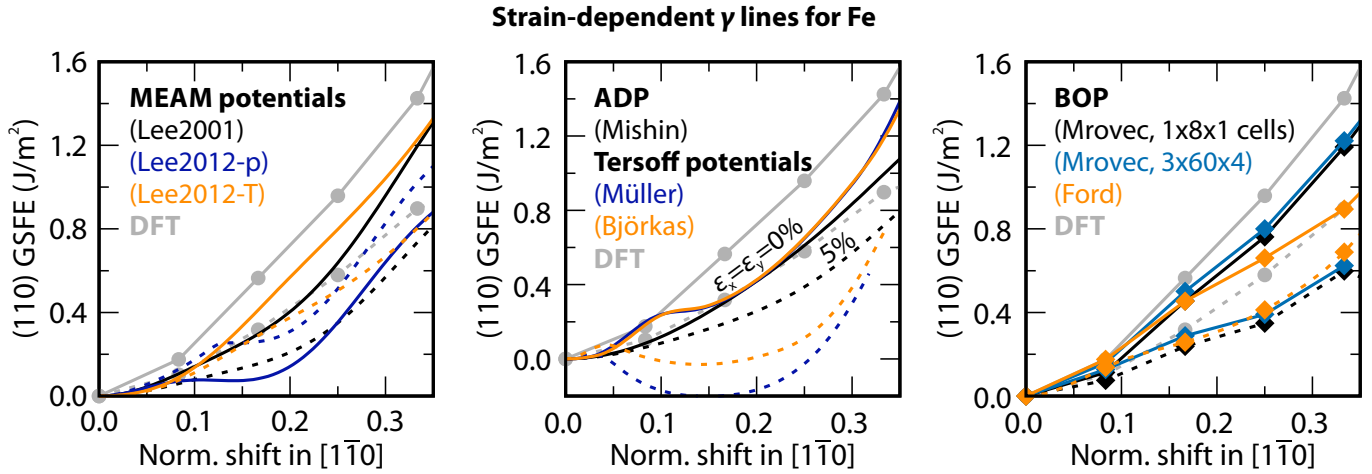


FIG. 4. Strain-dependent  $\gamma$  lines for Fe using MEAM, ADPs, and BOPs in comparison to the DFT (USPP) data. The GSFE data are plotted for 0% (solid lines) and 5% (dashed) applied equi-biaxial strain parallel to both the (110) plane normal and the  $[1\bar{1}0]$  shearing direction. The formation of a local GSFE minimum or at least a terrace at normalized shifts around 0.15 as observed for several EAM potentials (Figs. 3 and 5) is only observed for the Lee2012-p MEAM potential. In this case, the GSFE exhibits generally higher values for 5% than for 0% applied strains, which is attributed to a bcc  $\rightarrow$  hcp phase transformation for the unshifted configuration at 5% applied strain.

**Strain-dependent  $\gamma$  lines for bcc transition metals**

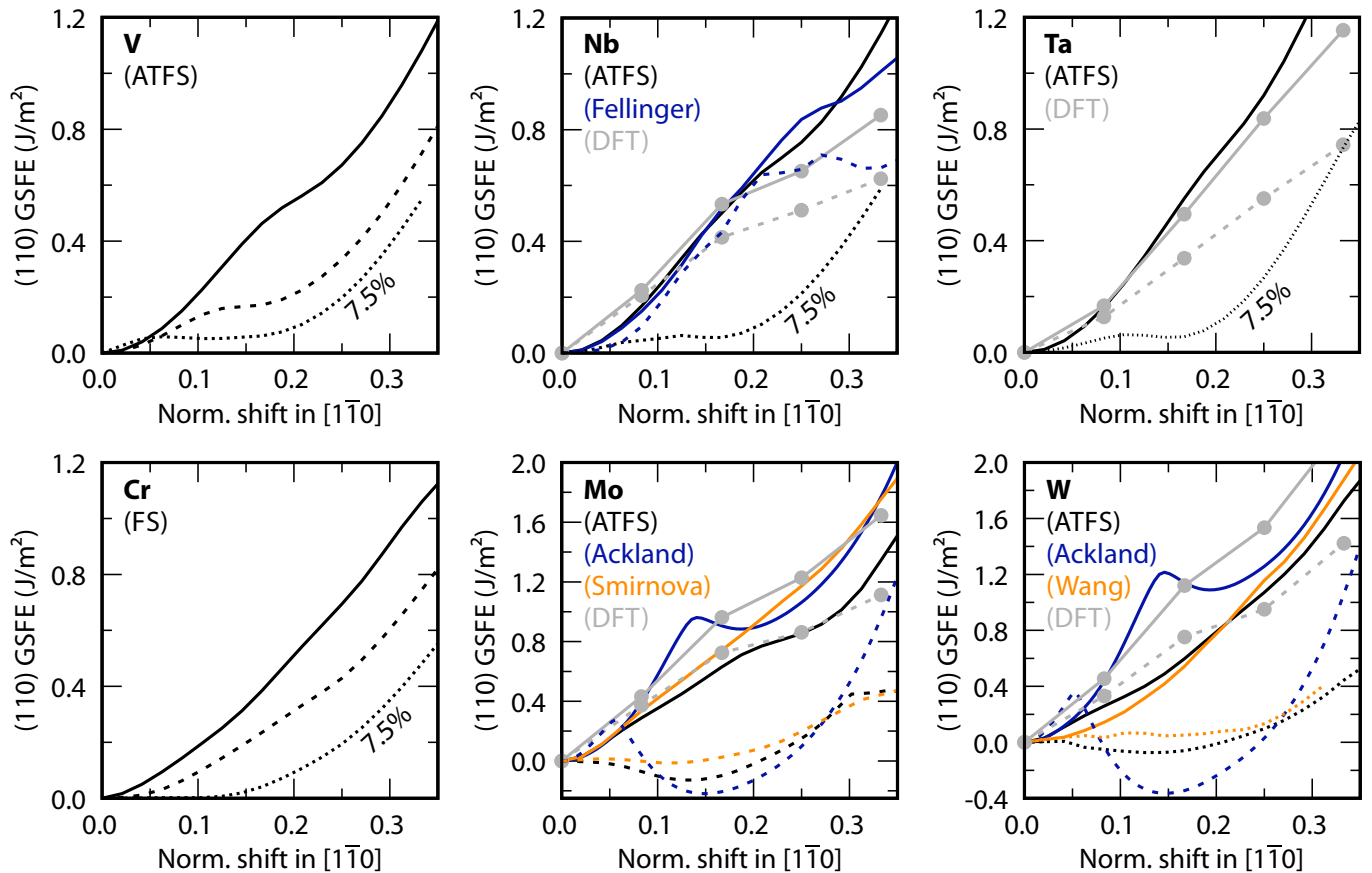


FIG. 5. Strain-dependent  $\gamma$  lines of various EAM potentials for the bcc metals V, Nb, Ta, Cr, Mo, and W. The GSFE data are plotted for 0% (solid lines), 5% (dashed), and 7.5% (dotted) applied equi-biaxial strain parallel to both the (110) plane normal and the  $[1\bar{1}0]$  shearing direction. The shift in  $[1\bar{1}0]$  direction is normalized, i.e., divided by the corresponding periodicity distance  $\sqrt{2}a_0$ . Relaxed stacking fault energies for Nb, Ta, Mo, and W were additionally calculated using DFT.

TABLE II. Overview of material models for bcc metals and presence (●) or absence (○) of a local  $\langle 110 \rangle$  GSFE minimum  $\min(\gamma_{[hkl]})$  where  $[hkl]$  is the shearing direction; US, uniaxial strain in  $[110]$  direction; EBS, equi-biaxial strain in  $[110]$  and  $[1\bar{1}0]$  direction;  $\rightarrow$ , largest strain studied.

Element (Potential)	Ref.	$\min(\gamma_{[111]})$		$\min(\gamma_{[110]})$		
		$\epsilon=0\%$	$\epsilon=0\%$	$\epsilon_{US}=7.5\%$	$\epsilon_{EBS}=5\%$	$\epsilon_{EBS}=7.5\%$
<i>Embedded Atom Method (EAM) Potentials</i>						
Fe (Mendelev-II) [34]		●	○	●	○	●
Fe (Chamati) [33]		○	○	○	○	●
Fe (Chiesa) [103, 104]		●	○	○	●	●
Fe (MFS) [49, 50]		○	○	○	○	●
Fe (Simonelli) [105]		○	○	○	○	●
Fe (Men-IIext) [106]		○	○	●	●	●
Fe (Gordon) [107]		○	○	○	○	●
Fe (Marinica07) [108]		○	○	○	○ <sup>a</sup>	○ <sup>a</sup>
Fe (Marinica11) [51]		●	○	●	○	●
V (ATFS) [49, 52]		●	○	—	○	●
Nb (ATFS) [49, 52]		●	○	—	○	●
Nb (Fellinger) [53]		○	○	—	●	●
Ta (ATFS) [49, 52]		○	○	—	○	●
Cr (FS) [49]		○	○	—	○	●
Mo (ATFS) [49, 52]		○	○	—	●	●
Mo (Ackland) [54, 55]		●	●	—	●	●
Mo (Smirnova) [56]		○	○	—	●	●
W (ATFS) [49, 52]		○	○	—	○	●
W (Ackland) [54, 55]		●	●	—	●	●
W (Wang) [57]		○	○	—	○	●
<i>Modified Embedded Atom Method (MEAM) Potentials</i>						
Fe (Lee2001) [63]		○	○	—	○	—
Fe (Lee2012-p) [65]		○	●	—	○ <sup>a</sup>	—
Fe (Lee2012-T) [65]		○	○	—	○	—
<i>Angular-Dependent Potential (ADP)</i>						
Fe (Mishin) [70]		○	○	—	○	—
<i>Tersoff Potentials</i>						
Fe (Müller) [76]		○	○	—	●	—
Fe (Björkas) [77]		○	○	—	●	—
<i>Bond-Order Potentials (BOP)</i>						
Fe (Mrovec) [79]		○	○	—	○	—
Fe (Ford) [84, 85]		○	○	—	○	—
<i>Density-functional theory (DFT) calculations</i>						
Fe (PAW-PBE) [99, 100]		○	○	○ ( $\rightarrow 10\%$ )	○	—
Fe (USPP-PBE) [95]		○	○	○ ( $\rightarrow 10\%$ )	○	○ ( $\rightarrow 22.5\%$ )
Nb (USPP-PBE) [95]		—	○	—	○	—
Ta (USPP-PBE) [91]		—	○	—	○	—
Mo (USPP-PBE) [95]		—	○	—	○	—
W (USPP-PBE) [95]		○	○	—	○	—

<sup>a</sup> original bcc lattice transformed to hcp lattice

presented for the more recent Chamati [33] and Chiesa potentials [104]. As expected from literature [94], the DFT results obtained with USPPs are in good agreement with the results for the more recent PAW method (see Supplemental Material).

It can clearly be seen that both the Mendelev-II and Chiesa potentials lead to local minima at normalized shifts in the range of 0.15 and 0.20 in the  $[1\bar{1}0]$ -direction. For the strain states shown in the figure, this was not the case for the Chamati potential and the DFT calculations. It is important to note that the shape of the GSFE curves for the Mendelev-II and Chiesa potentials differs qualitatively from the shape of the Chamati potential already at 0% strain [see Fig. 3(a)]. The

GSFE curves of the Mendelev-II and Chiesa potentials exhibit a consecutive change of curvature from positive to negative and back, which leads to a shoulder-like shape of the GSFE curve. By comparing the GSFE curves in Figs. 3(b) and 3(c), it can be seen that this "shoulder" often develops into a "hump" for applied strains. This "hump," which is identical to the formation of a local minimum, is shifted to smaller values of normalized shifts with increasing strain. Interestingly, this shoulder-like shape is also observed for relative shifts in the usual Burgers vector direction ( $[1\bar{1}1]$  direction, rightmost subfigures in Fig. 3). The Chamati potential, on the other hand, does initially not show such a shoulder, but starts to develop a similar shape at applied strains; see Figs. 3(b) and 3(c).

As it can be seen in Table II and in Fig. 3, the GSFE curves calculated with DFT methods do not develop a local minimum even for EBS values up to 10% whereas a local GSFE minimum occurs for the Chamati potential when the EBS was increased to 7.5%. The Chamati potential shares this behavior with all other EAM potentials. From the more sophisticated material models only the MEAM potential by Lee *et al.* ("Lee2012-p") and the Tersoff potentials by Müller *et al.* and Björkas *et al.* showed local minima (see Fig. 4). In the latter two cases, the minimum is not only local but *global*, which indicates the instability of the bcc phase under these conditions. For the other MEAM potentials as well as the ADP and BOPs local GSFE minima were not observed in the studied range of applied strains.

Figure 5 summarizes the resulting  $\gamma$  lines in the  $[1\bar{1}0]$  direction of the EAM potentials for the other bcc transition metals V, Nb, Ta, Cr, Mo, and W. In case of Nb, Ta, Mo, and W the results for the EAM potentials were compared to DFT calculations. Note that the EAM potentials for Cr (FS) and Mo (ATFS) show a completely different behavior for  $\epsilon_{[1\bar{1}0]} = \epsilon_{[110]} = 5\%$ . While the Mo potential shows a local (and even global minimum), no such minimum is observed for Cr. The non-physical predictions of the EAM potentials for Mo are in this case again confirmed by DFT calculations for the same strain state.

#### IV. DISCUSSION

Our results indicate that the observation of  $\{110\}$  planar faults—sometimes discussed as "fcc formation", see e.g. Refs. [22–25, 28, 31, 32]—is linked to the appearance of a local GSFE minimum under an applied strain. Zhang *et al.* already emphasized that the correct shape of GSFE curves is a challenge to empirical potentials [109]. In their work, the authors compared the GSFE curves for the  $\{112\}$  twin plane in the classical  $\langle 111 \rangle$  Burgers vector direction for five different interatomic potentials and DFT calculations for Nb. Similar to our work, some of the potentials lead to local GSFE minima at  $x \approx 1/3$  and  $2/3$  (where  $x$  corresponds to the shift in  $\langle 111 \rangle$  direction normalized to the Burgers vector length  $a_0/2\langle 111 \rangle$ ) for applied external strains. They showed that the trend to give a local GSFE minimum at applied strains correlates with the trend to give a local GSFE minimum in the  $\langle 111 \rangle$  Burgers

vector direction but at  $x = 1/2$  already at zero strain, leading to a double-hump shape of the GSFE. This observation is in contrast to our results where the focus is on the GSFE in  $\langle 110 \rangle$  directions (and on  $\{110\}$  planes) and where such a straightforward correlation is absent, cf. Table II. In other words, the formation of  $\{110\}$  PFs under applied strains is found to be independent of a double-hump GSFE at zero strain. Moreover, we applied comparably moderate *tensile* stresses around 20 GPa (for Fe) instead of 50 GPa *compressive* strains in the work by Zhang *et al.* In our work, the ATFS [49, 52] and Fellinger [53] potentials, which Zhang *et al.* found to reproduce the GSFE at applied strains for the  $\{112\}$  plane in the classical  $\langle 111 \rangle$  shearing direction, failed to do so for the  $\{110\}$  plane in  $\langle 110 \rangle$  shearing directions which are typically not subject to intense research efforts. It is therefore important to note, that an analysis of possible reasons for the occurrence of local GSFE minima at applied strains is currently lacking.

From a theoretical point of view, the occurrence of a local GSFE minimum is not expected in bcc materials. According to Neumann's principle [9], which states that the symmetry of physical properties is linked to the symmetry of the crystal, a local GSFE minimum (i.e. zero slope) would necessitate the crossing of two non-parallel mirror planes perpendicular to the studied glide plane. For bcc crystals at zero applied strains, this is clearly not the case while it is for fcc materials cf. Figs. 6(a) and Fig. 6(b). However, under conditions of extreme strains (e.g.  $\epsilon_{[1\bar{1}0]} = 22.5\%$ ) the  $\{111\}$  and  $\{112\}$  planes can become additional mirror planes of bcc crystals, [cf. Figs. 6(c) and Fig. 6(d)], thereby enabling the theoretical possibility of a local GSFE minimum. As it can be seen in the figure, only strains in the  $[1\bar{1}0]$  and  $[001]$  directions are needed for such a scenario, i.e., no strain perpendicular to the  $(100)$  PF plane is needed. On the other hand, some EAM potentials presented in Sec. III predict a GSFE minimum even if no strains are applied in these lateral directions but only in the  $[110]$  direction. We therefore conclude that the appearance of a local GSFE minimum does not occur for reasons of symmetry but is an unrealistic artifact rooted in the oversimplifications assumed to construct some of the material models. In particular, the strain-dependent formation of a local GSFE minimum was not observed for BOPs and in DFT calculations while it is predicted by all EAM and Tersoff potentials as well as for one MEAM potential (Lee2012-p). We further note that even for  $\epsilon_{[1\bar{1}0]} \approx 22.5\%$  and other scenarios of extreme applied strains, DFT calculations do not predict a local GSFE minimum as displayed in Fig. 6(e).

Why do certain models predict a local GSFE minimum and others do not? Although the statistical basis of our results is clearly not large enough to give a conclusive answer to this question, we can shed some light on it by analyzing the contributions that are explicitly included in the different material models (see Table I). Together with the results presented in Table II, this overview suggests that for obtaining an artifact-free GSFE surface the inclusion of direction-dependent bonding is a necessary—but not sufficient—condition. It is necessary since none of the EAM-type potentials (without direction dependence) results in an artifact-free behavior while some of the MEAM potentials (with direction dependence) do so.

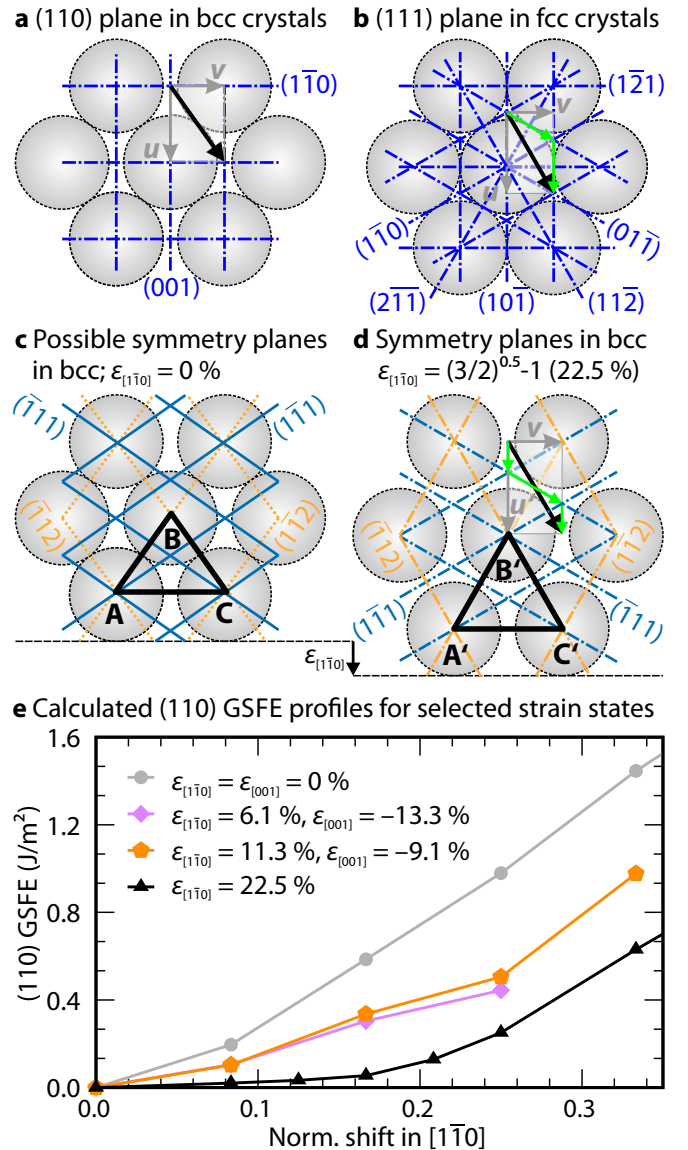


FIG. 6. Symmetry planes and Burgers vectors (black solid arrows) on the  $(110)$  slip plane in bcc (a) and the  $(111)$  slip plane in fcc crystals (b). Under zero-strain conditions, the  $\{111\}$  and  $\{112\}$  planes are no mirror planes of bcc crystals (c). Only if the crystal is strained in such a way that the isosceles triangle ABC becomes the equilateral triangle A'B'C' (d), then the  $\{111\}$  and  $\{112\}$  planes are mirror planes, form additional intersections, and the appearance of a local GSFE minimum is theoretically possible. The 1D GSFE profiles as calculated with DFT (e) for this (black symbols) and other extreme scenarios associated with an equilateral triangle A'B'C', however, do not predict a local GSFE minimum.

At the same time, it is only a sufficient condition since one MEAM and both Tersoff potentials (which both include direction dependencies) predict a local GSFE minimum. According to this analysis, it is not necessary to include electronic, magnetic, or bond-order effects to obtain a GSFE curve without a local minimum.

The failure of purely radial-symmetric functions to correctly describe the GSFE can generally be understood by the

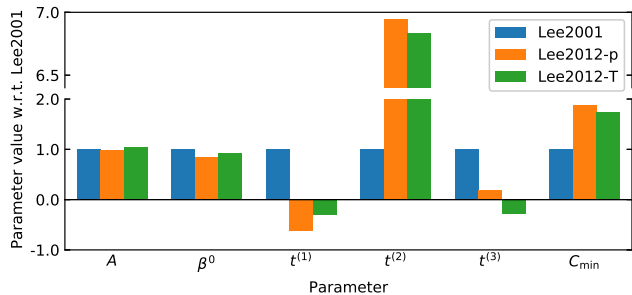


FIG. 7. Comparison of the parameters for the three MEAM potentials. The tendency to show a local GSFE minimum (in case of the Lee2012-p potential) correlates with the  $C_{\min}$  and  $t^{(2)}$  parameters and anti-correlates with the  $A$  and  $\beta^0$  parameters.

insufficient description of the nearest neighbor bonds in the EAM formalism when the atomic environment is deformed and difficulties in modeling situations where atoms leave or come within the interaction range of EAM potentials as, e.g., at surfaces, along transformation paths such as the Bain path, and in the case of GSFE surfaces. In a perfect crystal the contribution of further neighbor bonds is typically small (because the bond-order matrix elements of the further neighbors are significantly reduced). If, however, nearest neighbor atoms would be removed, the bond-order with further distant neighbors would increase. As the dependence of the strength of a bond on its local environment is not contained in the EAM, in order to suppress the formation of strong further distant bonds, EAM potentials have effectively to be cut off beyond the first or second neighbor shell of the equilibrium volume. Furthermore, the EAM formalism neglects the fact that the bond order may vary significantly between nearest neighbour bonds if an atom is not coordinated homogeneously.

It is also important to note that the material models which formally include direction dependence but give a local GSFE minimum, namely the MEAM and Tersoff potentials, still strongly rely on the contribution of pair potentials, e.g., of the Morse (Tersoff potential by Müller *et al.*[76]) or the Lennard-Jones type (ADP by Mishin *et al.*[70]). For both model types at least 10 parameters define the characteristics of the potential and it is difficult to deduce which of these is most responsible for the formation of a local GSFE minimum. However, the result that only the Lee2012-p MEAM potential[65] gives a local GSFE minimum opens the possibility to compare the changes made to its parameters with those parameters of the Lee2001 [63] and Lee2012-T [65] potentials which do not give a local GSFE minimum. Figure 7 compares the parameters that differ between these three MEAM potentials. From this comparison it can be seen that the tendency to lead to a local GSFE minimum correlates with the trend in the  $C_{\min}$  and  $t^{(2)}$  parameters and anti-correlates with the  $A$  and  $\beta^0$  parameters. This agrees well with the statement of Lee and Baskes [63] that the effect of changes in  $A$ ,  $\beta^0$  and  $C_{\min}$  on the elastic constants and the energy differences between bcc, fcc, and hcp can be significant. The analysis is, however, dramatically complicated by the distinct behavior of the Lee2012-p

potential, which transforms from bcc  $\rightarrow$  hcp already in the unshifted configuration at 5% equi-biaxial strain and gives an *increase* of the GSFE with applied strains, see Fig. 4. This transformation, however, is most likely not an artifact but due to its designation to reproduce the bcc-to-hcp transition pressure around 12 GPa (see Ref. [65]). For this reason, we can currently not propose a criterion for the tendency to form  $\{110\}$  PFs based on MEAM parameters.

We have also analyzed the training data that were used for parameterizing interatomic potentials as the training data generally determine the application range of a (material) model and it is therefore not *a priori* clear how it will respond to "unknown" scenarios. Due to the limited intrinsic transferability (as compared to BOP and DFT), the predictive power of classical potentials depends critically on the training set used during their parameterization. We noticed a vague trend that the inclusion of elastic constants, surface energies, and phase stabilities at the same time (this is the case for the Chamati-EAM, Lee2001-MEAM, and Mishin-ADP as well as for the BOPs) may be sufficient but not necessary (the MFS potential, for instance, was only fitted to elastic constants) for reducing the tendency to form a local GSFE minimum; see Supplemental Material for details.

Coming back to our initial statement about the importance of direction dependence, we now ask whether distance-dependent potential functions are really not sufficient to predict the correct shape of the strain-dependent GSFE surface or if the cutoff radii of the studied potentials (or their contributions due to pair interactions) were just too small. A too small cutoff radius may disable important interactions between atoms across the stacking fault plane when they are shifted relative to each other or when they are pulled apart by the application of external strains. However, the potentials with the smallest cutoff radius (MFS potential,  $r_{\text{cut}} = 3.4$  Å, including only first- and second-nearest neighbor interactions) and the largest cutoff radius (Chamati potential,  $r_{\text{cut}} = 5.67$  Å, including fifth-nearest neighbor interactions) both exhibit a similar behavior (local GSFE minimum at 7.5% equi-biaxial strain; see Table II). Therefore—although we cannot ultimately rule out this possibility—our results indicate that a too small cutoff radius is not responsible for the formation of a local GSFE minimum. A further indication for this conclusion is that third-nearest neighbor interactions are completely screened in the "Lee2012-T" MEAM potential [65] for which no local GSFE minimum is formed.

An alternative explanation for the failure of EAM potentials to predict the correct shape of GSFE surfaces may be found in the decomposition of their total energy into contributions by "pair" and "embedding" energies. This distinction, which dates back to the early days of the EAM formalism [35, 36], is somewhat arbitrary in more recently developed potential where potentials are obtained by the parameterizing, e.g., cubic spline functions; see, for instance, the Fe potentials in Refs. [34, 51, 103–105, 107, 108]. In Fig. 8 we compare the evolution of the "pair" and "embedding" contributions in dependence of the relative shift  $x$  for two interatomic potentials (Mendelev-II and Chamati) and the BOP by Mrovec *et al.* for which the "bond" energy is plotted instead of the "embed-

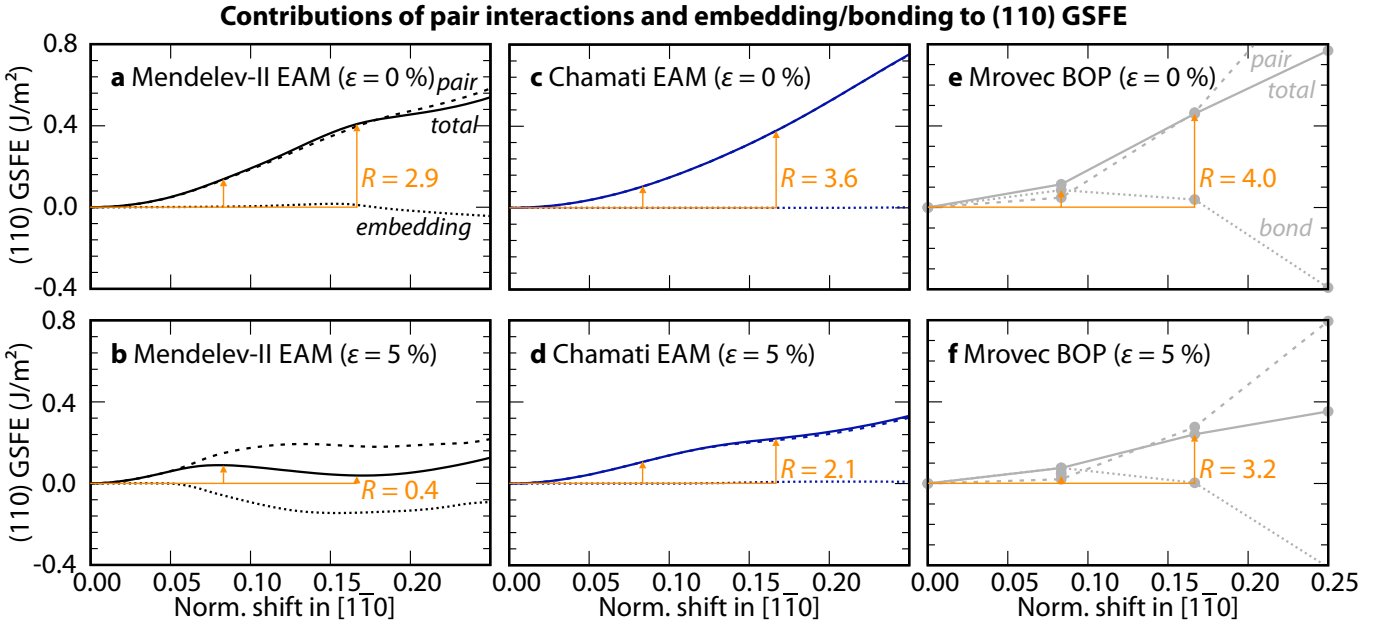


FIG. 8. (110) GSFE lines in  $[1\bar{1}0]$  direction decomposed in contributions of pair/embedding energy (EAM potentials) and pair/bond energy (BOP): (a) and (b), Mendeleev-II EAM potential; (c) and (d), Chamati EAM potential; (e) and (f), Mrovec BOP. The top (bottom) row shows the decomposed  $\gamma$  lines at 0% (5% equi-biaxial) strain. See Eq. (6) for the definition of  $R$ .

ding” energy. It can be seen that for all potentials the increase in total energy is mainly determined by pair interactions at zero strain and that the contribution of embedding/bond energy is negligible until approximately  $x = 1/6$ . When strains are applied (bottom row), this behavior persists only for the Chamati potential and the BOP [Figs. 8(d) and 8(f)]. For the Mendeleev-II potential, on the other hand, the total energy is lowered due to the increased (negative) contribution of the embedding energy [Fig. 8(b)] leading to the formation a local minimum. This observation suggests that an increasing contribution of the embedding energy under applied strains could be responsible for the formation of  $\{110\}$  PFs. As the individual contributions of pair/embedding energy depend, however, on the specific potential, this statement is not generalizable.

Under the assumption that first- and second-nearest neighbor interactions mainly determine the shape of the GSFE (as we have discussed before), we will now focus on their interactions across the sheared (110) plane. As we can see in Figs. 9(a)–9(c), each atom is interacting with two first-nearest neighbors (nn) and two second-nearest neighbors (2nn). Upon shifting the two half crystals, both nn bonds and one of the 2nn bonds are stretched while the other 2nn bond is compressed. For analyzing the energy contributions of these interactions, we make use of the effective pair potential format [110, 111], which overcomes the often arbitrary decomposition into “pair” and “embedding” contributions and thereby allows one to compare different EAM-type potentials on the same scale. More importantly this format offers a qualitative view on the energetics of pair interactions in a crystal (strictly, however, only for the perfect crystal structure and constant electron density). The effective pair potentials for the MFS, Mendeleev-II, and Chamati potentials are plotted in

Fig. 9(d). Since the energy change of the stretched 2nn bond is much larger than for the other bonds and the energy contributions of the nn bonds and the compressed 2nn bond nearly cancel out each other, the overall energetics of the GSFE must be dominated by the stretched 2nn bond. While being stretched, the energy contribution due to this bond is decaying and the contributions of the other bonds become more important. When external strains are applied, this transition takes place even earlier thereby opening the possibility that the stretched nn bonds or the compressed 2nn bond have not yet passed through the minimum (which lies between the nn and 2nn distance for most potentials). In such a case, the evolution of the total (GSFE) energy of the system would also pass through a (local) minimum.

The analysis of the nn and 2nn distances in Fig. 9(d) suggests that for an EAM-type potential to be robust against the formation of artificial  $\{110\}$  PFs, one of the neighbor distances (nn or 2nn) should be significantly further apart from the minimum under zero-strain conditions than the other (as for the Chamati potential). At the same time, the “tail” of the effective potential should monotonically increase to zero at large distance, i.e., without additional terrace points (e.g., Mendeleev-II, Mendeleev-IIext, and Marinica07). This recipe would also explain our previous observation that the cutoff radius does apparently not play a major role for the formation of  $\{110\}$  PFs. The plots of the effective pair potentials for the EAM-type Fe potentials can be found in the [Supplemental Material]. Although the effective pair potential is generally more suitable for a reliable and robust criterion than the decomposition into pair/embedding contributions, it has to be noted that there are also cases where this recipe does not work: Namely, in case of the FS potential for Cr where the minimum

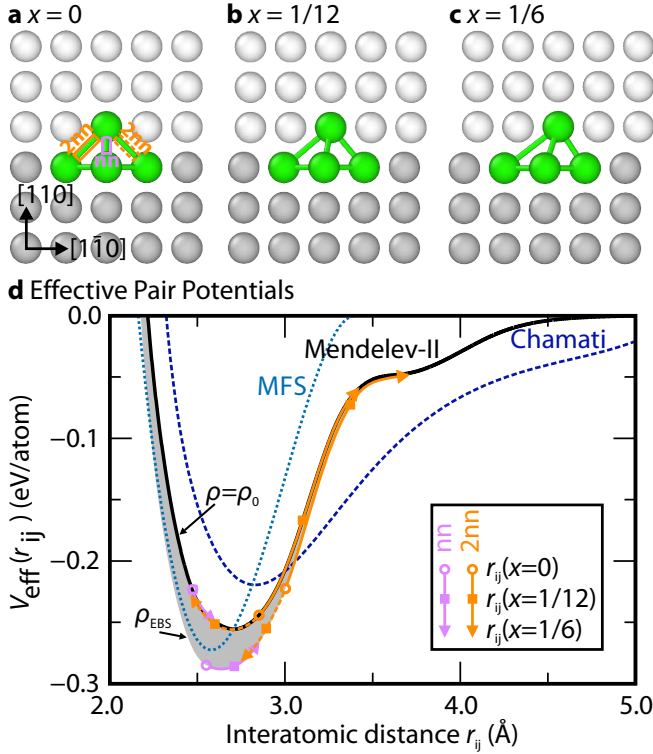


FIG. 9. Close-up views of the atomistic configurations at  $x = 0$  (a),  $x = 1/12$  (b), and  $x = 1/6$  (c) for the Mendeleev-II potential for Fe. For one atom in the upper half crystal, nn and 2nn neighbor atoms and the bonds between them are indicated in green color. The energy contributions due to the different neighbor distances are qualitatively compared using the effective pair potential ( $V_{\text{eff}}$ ) format (d). For comparison,  $V_{\text{eff}}(r_{ij})$  is also shown for the MFS and Chamati potentials, which are less prone to show a local GSFE minimum than the Mendeleev-II potential (see Table II). For the Mendeleev-II potential, the gray-shaded area indicates the change of  $V_{\text{eff}}$  for decreasing electron densities (corresponding to increasing applied strains). The nn and 2nn bonds and their evolution upon increasing strains  $x$  are shown with purple and orange lines, respectively, for zero strain (electron density  $\rho_0$ ) and 5% EBS ( $\rho_{\text{EBS}}$ ). While one 2nn bond is compressed [marked with a dashed line; see (a)], the other is stretched (solid line).

lies well-centered between the nn and 2nn distances but does not show the formation of  $\{110\}$  PFs.

To overcome the lack of robustness of the previously suggested recipes, we introduce an empirical but straightforward criterion for the tendency to form  $\{110\}$  PFs. An important feature of the potentials which exhibit a local GSFE minimum, which can be clearly observed in Figs. 3–5, is that the formation of a local GSFE minimum (or alternatively, the formation of a “hump”) at applied strains is linked to the formation of a “shoulder” under unstrained conditions (with “shoulder” we mean the region between two consecutive inflection points in the GSFE curves, where the curvature changes from positive to negative and back). The Mendeleev-II, Chiesa, Müller, and Björkas potentials for Fe and the Ackland potentials for Mo and W are prominent examples for this rather qualitative description, cf. Figs. 3 to 5. In an attempt to quantify this visual distinction between “hump” and “shoulder”,

TABLE III. Comparison of  $R$  [cf. Eq. (6)] for different material models for Fe.

Model	Parameter set	$R(\epsilon=0\%)$	$R(\epsilon_{\text{EBS}}=5\%)$
EAM	Mendeleev-II	2.9	0.4
EAM	Chamati	3.6	2.1
EAM	Chiesa	3.8	1.3
MEAM	Lee2001	2.8	2.6
ADP	Mishin	3.6	3.1
Tersoff	Björkas	1.6	1.4*
BOP	Mrovec	4.0	3.2
DFT	USPP-PBE	3.2	3.2

\* both  $\gamma(x = 1/6)$  and  $\gamma(x = 1/12)$  are negative

we calculate and compare the ratios

$$R = \frac{\gamma(x = 1/6)}{\gamma(x = 1/12)} \quad (6)$$

in Table III for selected material models for Fe and visualize them in Fig. 8 for the EAM potentials by Mendeleev *et al.* and Chamati *et al.* and the BOP by Mrovec *et al.*. When comparing the  $R$  values for the different models, it becomes evident that a significant decrease of  $R$  (more than 40%) from unstrained to strained conditions is indicative for the formation of a local GSFE minimum. Moreover,  $R < 2$  is a good indicator for a “shoulder” already under unstrained conditions, as, e.g., for the Björkas potential. An  $R$  value around or below unity is indicative for a “hump,” as e.g. for the Mendeleev-II and Chiesa potentials. This means, that for the future development of EAM potentials (and likewise for the pair-wise parts of MEAM, ADP and Tersoff potentials) it may be enough to ensure that  $R$  is well above 3 under unstrained and strained conditions which does not involve the calculation of the complete GSFE surface but only at  $x = 0, 1/12, \text{ and } 1/6$ .

Since we have not yet found a conclusive and generally applicable explanation for the formation of the local GSFE minimum under applied strains, we recommend including the determination of the strain-dependent  $\{110\}$  GSFE in the  $[1\bar{1}0]$  direction (or only the  $R$  value for reasons of efficiency) as a benchmark for newly developed potentials until the underlying reasons are clarified. For many practical applications, it may even be sufficient if  $R$  remains above 3 for equi-biaxial strains up to around 6%–7%. Potentials, which show PFs only at such high strains, can be seen as effectively artifact-free in this respect; see, e.g., the Chamati potential for Fe, which gives a local GSFE minimum at 7.5% equi-biaxial strain (cf. Table II), but no PFs under practical conditions (cf. Fig. 1), i.e., at crack tips.

## V. SUMMARY

In this study, we determined the strain dependence of the generalized stacking fault energy (GSFE) of  $\{110\}$  planes in bcc transition metals with different state-of-the-art material models for atomic-scale simulations: EAM and MEAM

potentials, ADPs, Tersoff potentials, BOPs, and DFT calculations. We showed that a number of EAM, MEAM, and Tersoff potentials predict an evolution of the strain-dependent  $\{110\}$  GSFE that exhibits a local minimum under applied uni- and equi-biaxial tensile strains resulting in the formation of planar faults (PFs), which are structurally very similar to the fcc structure. Examples for the formation of PFs in practice include simulations of cracks [22–29] and nanowires [30–32]. Since a local GSFE minimum under applied external strains is not observed with more sophisticated material models, i.e., DFT and BOPs, we conclude that the strain-dependent formation of PFs is an artifact of many classical potentials. For this reason, previous discussions based on observations of PFs (or misclassified fcc formations) in atomistic simulations can become questionable and should better be re-evaluated carefully.

We show that a local GSFE minimum is not formed for reasons of symmetry and that the inclusion of angular-dependent interaction terms is necessary but not sufficient for a material model to exhibit an artifact-free GSFE. For purely distance-dependent potentials, a too short cutoff radius is excluded as possible reason for the formation of  $\{110\}$  PFs. Instead, we find that the evolution of the effective pair potential for the next- and second-next-nearest neighbor distances can be

used to qualitatively understand the formation of a local GSFE minimum. Our attempts to develop a robust recipe to prevent this behavior were, however, not fully conclusive and we hope for future research in this direction. Until such a recipe is found, we recommend including the determination of the strain-dependent  $\{110\}$  GSFE (or the  $R$  value introduced in this paper) as a benchmark for newly developed potentials.

## ACKNOWLEDGEMENTS

J.J.M. gratefully acknowledges financial support of the Deutsche Forschungsgemeinschaft (DFG) via the research training group GRK 1896 "In Situ Microscopy with Electrons, X-rays and Scanning Probes." J.J.M. thanks B. Meyer for the pseudopotentials for Fe, Nb, Mo, and W, T. Klöffel for invaluable comments on the DFT calculations as well as J. Guénolé and W. G. Nöhring for technical support. T.H., R.D., and E.B. acknowledge financial support of the DFG through project C1 and C3 of the collaborative research centre SFB/TR 103 "From Atoms to Turbine Blades." I.B., T.H., and J.N. acknowledge financial support of the DFG within the SFB 761 "Steel—ab initio."

- 
- [1] Mishin Y, Asta M, Li J. Atomistic modeling of interfaces and their impact on microstructure and properties. *Acta Mater.* 2010;58:1117–1151.
  - [2] Needleman A, van der Giessen E. Micromechanics of Fracture: Connecting Physics to Engineering. *Mater Res Bull.* 2001;26:211–214.
  - [3] Leyson GPM, Curtin WA, Hector LG, Woodward CF. Quantitative prediction of solute strengthening in aluminium alloys. *Nat Mater.* 2010 sep;9(9):750–755. Available from: <http://www.nature.com/doi/10.1038/nmat2813>.
  - [4] Hasnaoui A, Van Swygenhoven H, Derlet PM. Dimples on Nanocrystalline Fracture Surfaces As Evidence for Shear Plane Formation. *Science.* 2003;300:1550–1552.
  - [5] Bitzek E, Brandl C, Weygand D, Derlet PM, Van Swygenhoven H. Atomistic simulation of a dislocation shear loop interacting with grain boundaries in nanocrystalline aluminium. *Modelling Simul Mater Sci Eng.* 2009;17:55008.
  - [6] Horstemeyer MF, Farkas D, Kim S, Tang T, Potirniche G. Nanostructurally small cracks (NSC): A review on atomistic modeling of fatigue. *Int J Fatigue.* 2010;32:1473–1502.
  - [7] Bitzek E, Gumbsch P. Mechanisms of Dislocation Multiplication at Crack Tips. *Acta Mater.* 2013;61:1394–1403.
  - [8] Vitek V. Intrinsic Stacking Faults in Body-centred Cubic Crystals. *Philos Mag.* 1968;18:773–785.
  - [9] Neumann FE. Vorlesungen über die Theorie der Elastizität der festen Körper und des Lichtäthers; 1885.
  - [10] Vitek V. Multilayer Stacking Faults And Twins on  $\{211\}$  Planes in B.C.C. Metals. *Scr Met.* 1970;4:725–732.
  - [11] Christian JW, Vitek V. Dislocations and stacking faults. *Reports Prog Phys.* 2002;33(1):307–411.
  - [12] Tschopp MA, McDowell DL. Tension-compression asymmetry in homogeneous dislocation nucleation in single crystal copper. *Appl Phys Lett.* 2007;90:121916.
  - [13] Brandl C, Derlet PM, Van Swygenhoven H. General-stacking-fault energies in highly strained metallic environments: Ab initio calculations. *Phys Rev B.* 2007;76(5):1–8.
  - [14] Kroupa F, Vitek V. Splitting of dislocations in b.c.c. metals on  $\{110\}$  planes. *Czech J Phys B.* 1964;14:337–346.
  - [15] Crussard C. Décomposition des dislocations dans le fer et les métaux cubiques centrés. *C R Acad Sci Paris.* 1961;252:273–275.
  - [16] Crussard C. Sur les défauts d'empilement dans le fer  $\alpha$ . *Acta Metall.* 1962;10:749–750.
  - [17] Cohen JB, Hinton R, Lay K, Sass S. Partial dislocations on the  $\{110\}$  planes in the b.c.c. lattice. *Acta Metall.* 1962;10:894–895.
  - [18] Kroupa F, Vitek V. Slip and the conception of splitting of dislocations in b.c.c. metals. *Can J Phys.* 1967;45:945–971.
  - [19] Bogers AJ, Burgers WG. Partial Dislocations on the  $\{110\}$  planes in the B.C.C. Lattice and the Transition of F.C.C. into the B.C.C. Lattice. *Acta Mater.* 1964;12:255–261.
  - [20] Smith DA, Gallot J. Dissociated Dislocations in Iron Observed by Field-Ion Microscopy. *Met Sci J.* 1969;3:79–80.
  - [21] Rothman RL, Cohen JB. X-Ray Study of Faulting in BCC Metals and Alloys. *J Appl Phys.* 1971;42:971–979.
  - [22] Latapie A, Farkas D. Molecular dynamics simulations of stress-induced phase transformations and grain nucleation at crack tips in Fe. *Modelling Simul Mater Sci Eng.* 2003;11:745–753.
  - [23] Borodin VA, Vladimirov PV. Molecular dynamics simulations of quasi-brittle crack development in iron. *J Nucl Mater.* 2011;415:320–328.
  - [24] Vatne IR, Østby E, Thaulow C. Multiscale simulations of mixed-mode fracture in bcc-Fe. *Modelling Simul Mater Sci Eng.* 2011;19:85006.
  - [25] Vatne IR, Østby E, Thaulow C, Farkas D. Quasicontinuum simulation of crack propagation in bcc-Fe. *Mater Sci Eng A.*

- 2011;528(15):5122–5134.
- [26] Möller JJ, Bitzek E. Comparative study of embedded atom potentials for atomistic simulations of fracture in  $\alpha$ -iron. *Modelling Simul Mater Sci Eng*. 2014;22:45002.
- [27] Tamer Al-Motasem A, Mai NT, Choi ST, Posselt M. Atomistic study on mixed-mode fracture mechanisms of ferrite iron interacting with coherent copper and nickel nanoclusters. *J Nucl Mater*. 2016; Available from: <http://linkinghub.elsevier.com/retrieve/pii/S0022314816300224>.
- [28] Ersland CH, Vatne IR, Thaulow C. Atomistic modeling of penny-shaped and through-thickness cracks in bcc iron. *Modelling Simul Mater Sci Eng*. 2012;20:75004.
- [29] Möller JJ, Bitzek E. On the influence of crack front curvature on the fracture behavior of nanoscale cracks. *Eng Fract Mech*. 2015;150:197–208.
- [30] Yang Y, Li S, Ding X, Sun J, Salje EKH. Interface Driven Pseudo-Elasticity in a-Fe Nanowires. *Adv Funct Mater*. 2016 feb;26(5):760–767. Available from: <http://onlinelibrary.wiley.com/doi/10.1002/adfm.201502488>.
- [31] Zhang Y, Yu DJ, Wang KM. Atomistic Simulation of the Orientation-dependent Plastic Deformation Mechanisms of Iron Nanopillars. *J Mater Sci Technol*. 2012 feb;28(2):164–168. Available from: <http://linkinghub.elsevier.com/retrieve/pii/S1538784X11001555>.
- [32] Skogsrud J, Thaulow C. Application of CTOD in atomistic modeling of fracture. *Eng Fract Mech*. 2015;150:153–160.
- [33] Chamati H, Papanicolaou NI, Mishin Y, Papaconstantopoulos DA. Embedded-atom potential for Fe and its application to self-diffusion on Fe(100). *Surf Sci*. 2006;600:1793–1803.
- [34] Mendelev MI, Han S, Srolovitz DJ, Ackland GJ, Sun DY, Asta M. Development of new interatomic potentials appropriate for crystalline and liquid iron. *Philos Mag*. 2003;83:3977–3994.
- [35] Daw MS, Baskes MI. Embedded-Atom Method: Derivation and application to impurities, surfaces, and other defects in metals. *Phys Rev B*. 1984;29:6443–6453.
- [36] Daw MS. Model of Metallic Cohesion: The Embedded Atom Method. *Phys Rev B*. 1989;39:7441–7452.
- [37] Möller JJ, Bitzek E. BDA: A novel method for identifying defects in body-centered cubic crystals. *Methods X*. 2016;3:279–288.
- [38] BDA. <http://jomoeller.github.io/bda>; Available from: <http://jomoeller.github.io/bda>.
- [39] Honeycutt JD, Andersen HC. Molecular dynamics study of melting and freezing of small Lennard-Jones clusters. *J Phys Chem*. 1987;91:4950–4963.
- [40] Bain EC. The Nature of Martensite. *Trans AIME Steel Div*. 1924;70:25–46.
- [41] Gilbert MR, Queyreau S, Marian J. Stress and temperature dependence of screw dislocation mobility in  $\alpha$ -Fe by molecular dynamics. *Phys Rev B*. 2011;84(17):1–11.
- [42] Coffman VR, Sethna JP, Heber G, Liu M, Ingraffea A, Bailey NP, et al. A comparison of finite element and atomistic modelling of fracture. *Modelling Simul Mater Sci Eng*. 2008;16:65008.
- [43] Tahir AM, Janisch R, Hartmaier A. Ab initio calculation of traction separation laws for a grain boundary in molybdenum with segregated C impurities. *Modelling Simul Mater Sci Eng*. 2013;21(7):16.
- [44] Ercolessi F, Adams JB. Interatomic Potentials from First-Principles Calculations: The Force-Matching Method. *Eur Lett*. 1994;26(8):583–588.
- [45] Paxton AT. Point, line and planar defects. In: Pettifor DG, Cottrell A, editors. *Electron theory Alloy Des*. Institute of Materials; 1992. p. 158.
- [46] Allen MP, Tildesley DJ. *Computer simulation of liquids*. Clarendon Press, Oxford; 1996.
- [47] OVITO. <http://ovito.org>;. Available from: <http://ovito.org>.
- [48] Stukowski A. Visualization and analysis of atomistic simulation data with OVITO - the Open Visualization Tool. *Modelling Simul Mater Sci Eng*. 2010;18:15012.
- [49] Finnis MW, Sinclair JE. A simple empirical N-body potential for transition metals. *Phil Mag A*. 1984;50:45–55.
- [50] Marchese M, Jacucci G, Flynn CP. Isotope effect of vacancy diffusion in b.c.c.  $\alpha$ -Fe. *Phil Mag Lett*. 1988;57:25–30.
- [51] Proville L, Rodney D, Marinica MC. Quantum effect on thermally activated glide of dislocations. *Nat Mater*. 2012;11:845–849.
- [52] Ackland GJ, Thetford R. An improved N-body semi-empirical model for body-centred cubic transition metals. *Philos Mag A*. 1987;56(1):15–30.
- [53] Fellingner MR, Park H, Wilkins JW. Force-matched embedded-atom method potential for niobium. *Phys Rev B*. 2010;81(14):1–15.
- [54] Han S, Zepeda-Ruiz LA, Ackland GJ, Car R, Srolovitz DJ. Interatomic potential for vanadium suitable for radiation damage simulations. *J Appl Phys*. 2003;93(6):3328–3335.
- [55] Ackland GJ. <http://www.homepages.ed.ac.uk/gja/moldy/AMISH.txt>; 2009. Available from: <http://www.homepages.ed.ac.uk/gja/moldy/AMISH.txt>.
- [56] Smirnova DE, Kuksin AY, Starikov SV, Stegailov VV, Insepov Z, Rest J, et al. A ternary EAM interatomic potential for UMo alloys with xenon. *Modelling Simul Mater Sci Eng*. 2013;21(3):35011. Available from: <http://stacks.iop.org/0965-0393/21/i=3/a=035011>.
- [57] Wang J, Zhou YL, Li M, Hou Q. A modified WW interatomic potential based on ab initio calculations. *Modelling Simul Mater Sci Eng*. 2014;22:15004.
- [58] Bitzek E, Gähler F, Hahn J, Kohler C, Krdzalic G, Roth J, et al. Recent developments in IMD: Interactions of covalent and metallic systems. In: Krause E, Jäger W, editors. *High Perform. Comput. Sci. Eng*. 2000. Springer, Heidelberg; 2001.
- [59] IMD. <https://github.com/itapmd/imd>; Available from: <https://github.com/itapmd/imd>.
- [60] Bitzek E, Koskinen P, Gähler F, Moseler M, Gumbsch P. Structural Relaxation Made Simple. *Phys Rev Lett*. 2006;97:170201.
- [61] Baskes MI. Modified embedded-atom potentials for cubic materials and impurities. *Phys Rev B*. 1992;46:2727.
- [62] Tadmor EB, Miller RE. *Modeling Materials: Continuum, Atomistic and Multiscale Techniques*. Cambridge University Press; 2011.
- [63] Lee BJ, Baskes MI, Kim H, Cho YK. Second nearest-neighbor modified embedded atom method potentials for bcc transition metals. *Phys Rev B*. 2001;64:184102.
- [64] Kim HK, Jung WS, Lee BJ. Modified embedded-atom method interatomic potentials for the FeTiC and FeTiN ternary systems. *Acta Mater*. 2009;57(11):3140–3147.
- [65] Lee T, Baskes MI, Valone SM, Doll JD. Atomistic modeling of thermodynamic equilibrium and polymorphism of iron. *J Phys Condens Matter*. 2012;24:225404.
- [66] Jelinek B, Groh S, Horstemeyer MF, Houze J, Kim SG, Wagner GJ, et al. Modified embedded atom method potential for Al, Si, Mg, Cu, and Fe alloys. *Phys Rev B*. 2012;85:245102.
- [67] Liyanage LSI, Kim SG, Houze J, Kim S, Tschopp MA, Baskes MI, et al. Structural, elastic, and thermal properties of cementite (Fe<sub>3</sub>C) calculated using a modified embedded atom method. *Phys Rev B*. 2014;89(9):094102. Available from:

- <http://link.aps.org/doi/10.1103/PhysRevB.89.094106> (Rev.) BCn 2006: nov;74(17):174117. Available from: <https://link.aps.org/doi/10.1103/PhysRevB.74.174117>
- [68] Plimpton S. Fast Parallel Algorithms for Short-Range Molecular Dynamics. *J Comp Phys*. 1995;117:1–19.
- [69] LAMMPS. <http://lammps.sandia.gov>; Available from: <http://lammps.sandia.gov>.
- [70] Mishin Y, Mehl MJ, Papaconstantopoulos DA. Phase stability in the Fe-Ni system: Investigation by first-principles calculations and atomistic simulations. *Acta Mater*. 2005;53:4029–4041.
- [71] Mishin Y, Lozovoi AY. Angular-dependent interatomic potential for tantalum. *Acta Mater*. 2006;54(19):5013–5026.
- [72] Hashibon A, Lozovoi AY, Mishin Y, Elsässer C, Gumbsch P. Interatomic potential for the Cu-Ta system and its application to surface wetting and dewetting. *Phys Rev B*. 2008;77:94131.
- [73] Mishin Y. "Our ADP Ta potential has a known error: the elastic constants predicted by the potential as a factor of two different from those reported in the paper. This was the result of a bug in the fitting code that was used during the potential development."; Available from: <https://www.ctcms.nist.gov/potentials/Ta.html>.
- [74] Tersoff J. New empirical model for the structural properties of silicon. *Phys Rev Lett*. 1986;56:632–635.
- [75] Morse PM. Diatomic Molecules According to the Wave Mechanics. II. Vibrational Levels. *Phys Rev*. 1929;34(1):57–64.
- [76] Müller M, Erhart P, Albe K. Analytic bond-order potential for bcc and fcc iron — comparison with established embedded-atom method potentials. *J Phys Condens Matter*. 2007;19:326220.
- [77] Björkas C, Nordlund K. Comparative study of cascade damage in Fe simulated with recent potentials. *Nucl Instruments Methods Phys Res Sect B Beam Interact with Mater Atoms*. 2007;259(2):853–860.
- [78] Henriksson KOE, Björkas C, Nordlund K. Atomistic simulations of stainless steels: a many-body potential for the Fe-Cr-C system. *J Phys Condens Matter*. 2013;25:445401. Available from: <http://www.ncbi.nlm.nih.gov/pubmed/24113334>.
- [79] Mrovec M, Nguyen-Manh D, Elsässer C, Gumbsch P. Magnetic bond-order potential for iron. *Phys Rev Lett*. 2011 jun;106(24):246402. Available from: <http://journals.aps.org/prl/abstract/10.1103/PhysRevLett.106.246402>.
- [80] Pettifor DG. New Many-Body Potential for the Bond Order. *Phys Rev Lett*. 1989;63:2480–2483.
- [81] Stoner EC. Collective Electron Ferromagnetism. II. Energy and Specific Heat. *Proc R Soc A*. 1939;169:339.
- [82] Drautz R, Hammerschmidt T, Čák M, Pettifor DG. Bond-order potentials: derivation and parameterization for refractory elements. *Modelling Simul Mater Sci Eng*. 2015 oct;23(7):074004. Available from: <http://stacks.iop.org/0965-0393/23/i=7/a=074004>.
- [83] Horsfield AP, Bratkovsky AM, Fearn M, Pettifor DG, Aoki M. Bond-order potentials: Theory and implementation. *Phys Rev B*. 1996;53(19):12694–12712. Available from: <http://link.aps.org/doi/10.1103/PhysRevB.53.12694>.
- [84] Ford ME, Drautz R, Hammerschmidt T, Pettifor DG. Convergence of an analytic bond-order potential for collinear magnetism in Fe. *Modelling Simul Mater Sci Eng*. 2014 apr;22(3):034005. Available from: <http://stacks.iop.org/0965-0393/22/i=3/a=034005>.
- [85] Madsen GKH, McEniry EJ, Drautz R. Optimized orthogonal tight-binding basis: Application to iron. *Phys Rev B*. 2011;83(18):1–7.
- [86] Drautz R, Pettifor DG. Valence-dependent analytic bond-order potential for transition metals. *Phys Rev B*. 2006; nov;74(17):174117. Available from: <https://link.aps.org/doi/10.1103/PhysRevB.74.174117>.
- [87] Hammerschmidt T, Seiser B, Ford ME, Ladines AN, Schreiber S, Wang N, et al.. BOPfox program for tight-binding and bond-order potential calculations, submitted;. Available from: <https://arxiv.org/abs/1803.07491>.
- [88] Hohenberg P. Inhomogeneous Electron Gas. *Phys Rev*. 1964 nov;136(3B):B864–B871. Available from: <http://journals.aps.org/pr/abstract/10.1103/PhysRevB.136.864>.
- [89] Kohn W, Sham LJ. Self-Consistent Equations Including Exchange and Correlation Effects. *Phys Rev*. 1965 nov;140(4A):A1133–A1138. Available from: <http://journals.aps.org/pr/abstract/10.1103/PhysRevB.140.1133>.
- [90] Giannozzi P, Baroni S, Bonini N, Calandra M, Car R, Cavazzoni C, et al. Quantum ESPRESSO: a modular and open-source software project for quantum simulations of materials. *J Phys Condens Matter*. 2009;21(39):395502 (19pp).
- [91] Quantum ESPRESSO. <http://www.quantum-espresso.org/>; Available from: <http://www.quantum-espresso.org/>.
- [92] Perdew JP, Burke K, Ernzerhof M. Generalized Gradient Approximation Made Simple. *Phys Rev Lett*. 1996 oct;77(18):3865–3868. Available from: <http://journals.aps.org/prl/abstract/10.1103/PhysRevLett.77.3865>.
- [93] Vanderbilt D. Soft self-consistent pseudopotentials in a generalized eigenvalue formalism. *Phys Rev B*. 1990 apr;41(11):7892–7895. Available from: <http://journals.aps.org/prb/abstract/10.1103/PhysRevB.41.7892>.
- [94] Ventelon L, Willaime F. Generalized stacking-faults and screw-dislocation core-structure in bcc iron: A comparison between ab initio calculations and empirical potentials. *Philos Mag*. 2010;90:1063–1074.
- [95] Meyer B. Private communication; 2014.
- [96] Monkhorst HJ, Pack JD. Special points for Brillouin-zone integrations. *Phys Rev B*. 1976 jun;13(12):5188–5192. Available from: <http://journals.aps.org/prb/abstract/10.1103/PhysRevB.13.5188>.
- [97] Fu CL, Ho KM. First-principles calculation of the equilibrium ground-state properties of transition metals: Applications to Nb and Mo. *Phys Rev B*. 1983 nov;28(10):5480–5486. Available from: <http://journals.aps.org/prb/abstract/10.1103/PhysRevB.28.5480>.
- [98] Press WH. Numerical Recipes 3rd Edition: The Art of Scientific Computing. Cambridge University Press; 2007. Available from: <https://books.google.com/books?id=1aA0dzK3FegC>.
- [99] Kresse G, Hafner J. Ab initio molecular dynamics for liquid metals. *Phys Rev B*. 1993 jan;47(1):558–561. Available from: <http://journals.aps.org/prb/abstract/10.1103/PhysRevB.47.558>.
- [100] VASP. <http://www.vasp.at>; Available from: <http://www.vasp.at>.
- [101] Kresse G, Joubert D. From ultrasoft pseudopotentials to the projector augmented-wave method. *Phys Rev B*. 1999 jan;59(3):1758–1775. Available from: <http://link.aps.org/doi/10.1103/PhysRevB.59.1758>.
- [102] Bleskov I, Hickel T, Neugebauer J, Ruban A. Impact of local magnetism on stacking fault energies: A first-principles investigation for fcc iron. *Phys Rev B*. 2016 jun;93(21):214115. Available from: <http://link.aps.org/doi/10.1103/PhysRevB.93.214115>.
- [103] Dudarev SL, Derlet PM. A 'magnetic' interatomic potential for molecular dynamics simulations. *J Phys Condens Matter*. 2005;17:7097–7118.

- [104] Chiesa S, Derlet PM, Dudarev SL, Van Swygenhoven H. Optimization of the magnetic potential for  $\alpha$ -Fe. *J Phys Condens Matter*. 2011;23:206001.
- [105] Simonelli G, Pasianot R, Savino EJ. Embedded-atom-method interatomic potentials for bcc-iron. *Mater Res Soc Symp Proc*. 1993;291:567–572.
- [106] Ackland GJ, Mendelev MI, Srolovitz DJ, Han S, Barashev A. Development of an interatomic potential for phosphorus impurities in alpha-iron. *J Phys Condens Matter*. 2004;16:S2629–S2642.
- [107] Gordon PA, Neeraj T, Mendelev MI. Screw dislocation mobility in BCC Metals: a refined potential description for  $\alpha$ -Fe. *Philos Mag*. 2011;91:3931–3945.
- [108] Malerba L, Marinica MC, Anento N, Björkas C, Nguyen H, Domain C, et al. Comparison of empirical interatomic potentials for iron applied to radiation damage studies. *J Nucl Mater*. 2010;406:19–38.
- [109] Zhang RF, Wang J, Beyerlein IJ, Germann TC. Twinning in bcc metals under shock loading: a challenge to empirical potentials. *Philos Mag Lett*. 2011 dec;91(12):731–740. Available from: <http://www.tandfonline.com/doi/abs/10.1080/0950083>
- [110] Gordon PA, Neeraj T, Luton MJ, Farkas D. Crack-Tip Deformation Mechanisms in  $\alpha$ -Fe and Binary Fe Alloys: An Atomistic Study on Single Crystals. *Met Mater Trans A*. 2007;38:2191–2202.
- [111] Johnson RA. Alloy models with the embedded-atom method. *Phys Rev B*. 1989;39:12554.